

On the Rivers in the Euro-Atlantic Sky

Venugopal Thandlam (✉ venux4@gmail.com)

Uppsala University <https://orcid.org/0000-0001-7771-1693>

Anna Rutgersson

Uppsala University, Centre of Natural Hazards and Disaster Science

Erik Sahlee

Uppsala University

Article

Keywords: Atmospheric Rivers, north Atlantic Ocean, summer half-year, winter half-year, geopotential, surface latent heat flux, North Atlantic Oscillation and Scandinavian blocking

Posted Date: August 14th, 2020

DOI: <https://doi.org/10.21203/rs.3.rs-48633/v2>

License:  This work is licensed under a Creative Commons Attribution 4.0 International License.

[Read Full License](#)

Abstract

We study and revisit the Atmospheric Rivers (AR) over Euro-Atlantic sky using long term reanalysis datasets and widely used methods and parameters. The atmospheric winds, temperature and specific humidity at different pressure levels during 1979-2018 were used to study the spatiotemporal variability of water vapour transport integrated between 1000-300 hPa (IVT300) as a proxy to ARs. The standard deviation ($200 \text{ kgm}^{-1}\text{s}^{-1}$) of ARs is around 60% of the climatology ($>300 \text{ kgm}^{-1}\text{s}^{-1}$) in all reanalysis datasets in the North Atlantic. High frequency of ARs over western Europe in winter half-year (WHY) has 6% lower intensity compared to the low frequency of ARs in summer half-year (SHY) with 3% higher intensity than the annual mean. The intensity of ARs in the North Atlantic has been increasing in recent times with large decadal variability and poleward shift in landfalling. The magnitude of atmospheric parameters in the lower atmosphere below 750 hPa dominates the total column water vapour and intensity of ARs. There is a significant impact of the North Atlantic Oscillation and Scandinavian blocking on the location of landfalling of ARs and latitudinal dependence of the source of moisture flux in the open ocean contributing to the formation and enhancing ARs strength.

Introduction

Tropospheric atmospheric dynamics are guided by water vapour in the lower atmosphere (Schneider et al., 1999). Particularly, heat and momentum in the lower troposphere have strong coupling with the movement of moisture in the troposphere. Hence, it is essential to study the tropospheric moisture transport to better understand the global water cycle, synoptic weather patterns and climate change due to enhanced evaporation in recent decades due to global warming (Trenberth, 2011). Also, the ocean and atmosphere play a key role in transporting heat and water vapour poleward, respectively. Atmospheric general circulation plays a vital role in circulating water vapour in the lower troposphere. The large-scale land-ocean atmospheric exchange of water demonstrates the coupling of the atmospheric branch of the hydrological cycle (Hack et al., 2006). The global and continental-scale transport of water vapour has important implications for climate variability and hydrology (Brubaker et al., 1994). Hence, atmospheric scientists must consider studying climatological, meteorological and hydrological aspects of the transport of moisture in the lower atmosphere (Gimeno 2013; Gimeno et al., 2012). It is particularly important to understand the conceptual models of moisture transport to aid research into the origin of continental precipitation (Gimeno 2014). Also, moisture transport in mid-latitudes plays a key role in guiding the global atmosphere and climate dynamics in various temporal and spatial scales.

Most of the meridional water vapour transported across the midlatitudes (90% of the total mid-latitude vertically integrated water vapour flux) takes place through narrow corridors in less than 10% of the zonal circumference called atmospheric rivers (ARs) (Yong and Newell 1998; Ralph et al. 2004). These transient filamentary regions occur within the warm conveyor belt of extratropical cyclones in a maritime environment and are characterized by high water vapour content and strong low-level winds (Ralph et al. 2004, 2005, 2006). Thus, these corridors tend to be quite narrow ($<1000 \text{ km}$ wide) relative to their length scale ($>2000 \text{ km}$) (Neiman et al., 2008). The warm conveyor belt transports both sensible and latent heat,

particularly the later contributes to the poleward heat transport that occurs in the form of water vapour flux from the warm sea surface over oceanic regions serving as a major moisture source. Most of the water vapour transport within these rivers occurs in the lowest 2.5 km of the atmosphere due to moist-neutral stratification (Ralph et al. 2005). Hence, these are also called tropospheric rivers due to their occurrence in the lower troposphere (Yong and Newell 1994, 1998). The combination of lower-tropospheric moist neutrality, strong horizontal winds, large and concentrated water vapour content yields occurrence of heavy orographic precipitation and winds on elevated terrain lead to heavy flooding (Ralph et al. 2006; Neiman et al. 2002, 2011; Ruby and Qian 2009, Lavers et al., 2011, 2012; Waliser and Guan 2017), which could further cause landslides to occur over the adjacent area (Jason et al., 2019). Heavy and untimely precipitation (Kritika et al., 2018; Yan et al., 2018) from warm ARs also causes preexisting snowpack to melt at the high latitudes and poles allowing freshwater inflow into the oceans and contribute to the sea level rise (Neff William 2018; Mattingly et al., 2018), leading to coastal flooding (Khouakhi and Villarini 2016). Snowmelt and intense flooding due to ARs could change the geomorphic processes, biodiversity and mass mortality of wildlife (Joan et al., 2015; Brian et al., 2016). Conversely, ARs could also change the ice sheet surface mass balance over the poles by 74-80% through heavy snow accumulation (Irina et al., 2014). Thus, ARs are key to understanding extratropical and polar hydroclimate features through polar warming, sea ice melt, and precipitation (Deanna et al., 2018; Kensuke et al., 2018). Consequently, these mesoscale filamentary features play a crucial role in the global water cycle and represent a key phenomenon linking weather and climate.

There are numerous studies over midlatitudes documenting the AR characteristics, landfall, and their relationship with the extreme hydrometeorological events. Many studies have focused on the ARs over Pacific; particularly on the south-west coast of the United States (Ralph et al., 2006, 2019, 2005, 2006; Neiman et al., 2008; Chapman et al., 2019, and the references therein) and South America (Viale and Nunez, 2011). There are a few studies aimed at the global characteristics of ARs (Waliser and Guan 2017; Guan and Waliser 2017, 2015). Recently there is an increasing focus on the precipitation over Europe and ARs over the north Atlantic (Pasquier et al., 2019; Yang et al., 2016; Lavers et al., 2016; Champion et al., 2015). Recent studies in Asia (Kritika et al., 2018; Yang et al., 2018; Youichi et al., 2017) and Africa (Blamey et al., 2018; Alexandre et al., 2018) have focused on the relationship between ARs and the extremes in precipitation. However, the study of ARs over the north Atlantic and Europe needs more attention due to increasing extremes in hydrometeorological events such as snowfall, precipitation and flooding; and changes in hydrological cycles over Europe causing large socio-economic damages (Millán 2014; Kundzewicz et al., 2006; Van den Besselaar et al., 2013). Majority of extreme wind events catalogued between 1997 and 2013 over Europe with billion US dollar losses were associated with ARs (Waliser and Guan 2017). Hence, it is essential to study both oceanic and atmospheric processes affecting these anomalies and extremes. AR is one such feature which is guided by both oceanic and atmospheric dynamics and causes extremes in precipitation and influences the hydrology over Europe. Lavers et al., (2013) studied the relationship between ARs and extreme precipitation across Europe and found that North Atlantic Oscillation has a significant impact on precipitation caused by ARs. The same study highlighted the anomalies in central European precipitation patterns caused by ARs over the north

Atlantic. According to a multi-model ensemble of the Coupled Model Intercomparison Project (CMIP5); AR frequency is projected to increase 127%-275% by the end of this century, at peak AR frequency regions (45°-55°N) over Europe, assuming the representative concentration pathway 8.5 (RCP8.5) scenario. This enhanced frequency is associated with the wind changes in the midlatitude jet (Yang et al., 2016). ARs cause 20-30% of all precipitation in parts of Europe and the United States with strong seasonality in precipitation. Also, ARs penetrate further inland over Europe than over the United States (Lavers and Villarini 2015). On the other hand, ARs are in sync with the largest floods over western Europe and the United Kingdom (Lavers et al., 2011, 2012).

Several procedures are in practice to detect, track and forecast ARs in advance using observational, reanalysis, and numerical models (Ralph et al., 2019; Fish et al., 2019; Lavers et al., 2018). Integrated Water Vapor (IWV) (Ralph et al., 2004; Neiman et al., 2008b; Guan et al., 2010) and integrated vapour transport (IVT) (Zhu and Newell, 1998; Roberge et al., 2009; Jiang and Deng, 2011) are the two most common techniques used to detect and track the ARs. Time integrated IVT, Meteograms and cross-sections are some of the other methods to study ARs. Both IWV and IVT consider vertically integrated (between 1000 hPa to 300 hPa or less) horizontal water vapour transport (significant poleward moisture transport) as a proxy to AR occurrence when the standardized IVT was greater than a threshold (Roberge et al. 2009). Accurate atmospheric parameters such as winds, specific humidity, and the temperature at different pressure levels obtained from satellites and reanalysis products are essential to study the ARs (Neiman et al., 2009; Dettinger, 2011). Though the necessary parameters are available from different platforms, atmospheric reanalysis is the best estimate of the historical state of the Earth's atmosphere. These datasets are produced by assimilating meteorological/oceanic observations into numerical weather prediction model output. In this work, we aim to study the characteristics of ARs over the north Atlantic by revisiting the widely used methods and parameters. The objective of this study is also to look at the variability of ARs in the north Atlantic in relation to the different ocean and atmospheric parameters. We also focus on the resolution dependence of ARs over the north Atlantic. The paper is organized as follows. Section 2 describes the data and methods, followed by results and discussions in section 3 and conclusions in section 4.

Methods

In the present study, we have used six-hourly winds, temperature, and specific humidity data at different pressure levels from six reanalysis products available until 2018. These six reanalysis datasets include 20th Century Reanalysis version 2 (20CR-V2) from the NOAA Earth System Research Laboratories (ESRL), ERA-Interim, ERA5 from the European Centre for Medium-Range Weather Forecasts (ECMWF), Modern-Era Retrospective analysis for Research and Applications (MERRA-2) from National Aeronautics and Space Administration (NASA), Climate Forecast System Reanalysis version 2 (CFSR-v2), NCEP-NCAR Reanalysis version 2 from the National Centers for Environmental Prediction (NCEP). Apart from MERRA-2, which has been available since 1980; all datasets are available from 1979 and have different spatial resolutions. Complete details of the reanalysis datasets used in the study are given in table 1. In addition to traditionally mapping ARs using both IVT (Equation 1) and IWV (Equation 3), we also included

temperature of corresponding layers in these algorithms to normalize the computed IVT (nIVT, Equation 2) and IWV (nIWV, Equation 4) and study the difference from the normal approach using different reanalysis products and compared these two methods in the Atlantic.

Integrated Vapor Transport (IVT):

$$IVT = g^{-1} \sqrt{\left(\int_{1000}^p QU dp\right)^2 + \left(\int_{1000}^p QV dp\right)^2} \quad (1)$$

Normalized IVT:

$$nIVT = g^{-1} \sqrt{\left(\int_{1000}^p \frac{QU}{T} dp\right)^2 + \left(\int_{1000}^p \frac{QV}{T} dp\right)^2} \quad (2)$$

Integrated Water Vapor (IWV):

$$IWV = g^{-1} \int_{1000}^p Q dp \quad (3)$$

Normalized IWV:

$$nIWV = g^{-1} \int_{1000}^p \frac{Q}{T} dp \quad (4)$$

Where Q is specific humidity in kgkg^{-1} , U and V are zonal and meridional components of winds at different pressure levels measured in ms^{-1} , P is the desired pressure (hPa) up to which the atmospheric parameters are integrated; g is the acceleration due to gravity, which is a constant and is given as 9.8 ms^{-2} . Normalization with temperature is done by dividing the two terms inside the square brackets with the temperature at a corresponding pressure level. Table 2 shows the details of the variables and their units.

Thus, time-integrated (4 time-steps) daily ARs data has been generated from six-hourly reanalysis datasets using IVT ($\text{kgm}^{-1}\text{s}^{-1}$), normalized IVT ($\text{kgm}^{-1}\text{s}^{-1}\text{K}^{-1}$); IWV (mm) and normalized IWV (mmK^{-1}) from the surface to 750 hPa, 500 hPa and 300 hPa. Temperature normalization is done to understand the change in the thermodynamic component of IVT and IWV using the Clausius-Clapeyron equation (3), which states that the water-vapour content of saturated air, q^* , increases nearly exponentially with temperature T (Payne et al., 2020).

$$\frac{dq^*}{dT} = \alpha(T)q^* \quad (3)$$

$\alpha(T)$ is the Clausius-Clapeyron scaling factor, defined as

$$\alpha(T) = \frac{L}{R_v T^2}$$

where L is the latent heat of vaporization and R_v is the gas constant of water vapour. Within the saturated environment at the core of an AR where $q \approx q^*$, a small change in the surface warming would cause specific humidity to further enhance. Thus, specific humidity in the upper layers of the atmosphere strongly depends on the increase in layer's temperature with respect to surface temperature and the Clausius-Clapeyron scaling factor, $\alpha(T)$ and is approximately $6.6\% \text{ K}^{-1}$ for surface temperatures causing ARs that are landfalling over California in the present climate ($T = 13^\circ\text{C}$) (Dettinger 2011; Gonzales et al., 2019).

The time-integrated (6-hourly) daily AR data has been used in further analysis to study the temporal and spatial variability of ARs over the north Atlantic both in climatic and decadal timescales. In addition to studying the biases in different atmospheric parameters, the annual and seasonal climatology and strength of the ARs at different layers were studied. For the intercomparing of reanalysis datasets, we consider ERA5 as the reference dataset. Furthermore, the study focuses on the variability of ARs intensities in different products including major categories of ARs and their frequencies in the north Atlantic. Regression analysis done helps to understand the spatial trend in the ARs, followed by studying the state of the atmosphere using major atmospheric parameters describing the characteristics of the occurrence of ARs.

Table 1: Details on the reanalysis datasets used in the present study

Dataset	Source	Availability	Temporal Resolution	Spatial Resolution	Reference
20th Century Reanalysis (20CR-V2)	ESRL: PSD/NOAA	1851-2014	6 hourly	2 x 2 x 24, 1000 - 10 hPa	Compo et al., (2011)
ERA-Interim	ECMWF	1979-present	6 hourly	0.75 x 0.75 x 60, 1000 - 0.1 hPa	Dee et al., (2011)
ERA5	ECMWF	1979-present	6 hourly	0.25 x 0.25 x 37, 1000 - 1 hPa	Hersbach, H et al., (2017)
Modern-Era Retrospective analysis for Research and Applications (MERRA-2)	Global Modelling and Assimilation Office (NASA)	1980-present	6 hourly	0.5 x 0.625 x 42, 1000 - 1 hPa	Gelaro et al., (2017)
Climate Forecast System Reanalysis (CFSR-v2)	National Centers for Environmental Prediction (NCEP)	1979-present	6 hourly	38 x 64 km, 1000-0.266 hPa	Saha et al., (2014)
NCEP-NCAR Reanalysis - v2	NCEP-NCAR	1979-present	6 hourly	2.5 x 2.5 x 28, 1000 - 3 hPa	Kanamitsu et al., (2002)

Table 2: Details of the variables and their units used in the study.

Parameter/Description	Variable	Units
Zonal wind	U	ms ⁻¹
Meridional wind	V	ms ⁻¹
Temperature	T	Kelvin
Specific humidity	Q	kgkg ⁻¹
Integrated Vapor Transport	IVT	kgm ⁻¹ s ⁻¹
Normalized Integrated Vapor Transport	nIVT	kgm ⁻¹ s ⁻¹ K ⁻¹
Integrated Water Vapor	IWV	mm
Normalized Integrated Water Vapor	nIWV	mmK ⁻¹
Mean Sea level pressure	P	hPa
Geopotential	φ	m ² s ⁻²
Surface latent heat flux	L	Wm ⁻²

Results And Discussion

Climatology and standard deviation of ARs over the north Atlantic:

Quantification of ARs over the north Atlantic was done using the climatology and standard deviation for different methods. This is essential to see the spatial variability including the magnitude of water vapour transport over the north Atlantic and into western Europe. The climatology from ERA5 daily data using IVT and nIVT methods shows highest AR intensity in the region enclosed between 30°N-60°N (Figure 1). Though the intensity of AR varies from event to event, on average IVT300 (IVT between 1000-300 hPa) (Figure 1a) over the north Atlantic is around 300 kgm⁻¹s⁻¹ and is in line and directed along with the westerly wind over this region. The maximum nIVT300 (nIVT between 1000-300 hPa) over the north Atlantic is in coherence with the maximum IVT300 and along the same path with maximum values (>1 kgm⁻¹s⁻¹K⁻¹) concentrated over central North Atlantic (Figure 1b). The nIVT300 is accounted for available IVT300 per unit temperature is a proxy to the fractional changes in available specific humidity in the atmospheric column per degree of atmospheric warming. In the upper layers of the atmosphere, α varies with the varying temperature. Hence, α increases with the decreasing temperature with height and amplifies the changes in the specific humidity aloft and is larger in the upper troposphere. On the other hand, increasing specific humidity in the upper layers tends to release more latent heat flux with ascending air, and decrease the lapse rate with warming and thus increasing the temperature with height. If the vertical column of the atmosphere is saturated and has moist-neutral conditions, the combination of these factors implies a rate increase in IVT that is substantially larger than that of near-surface water vapour (Payne et al., 2020). Hence, the fractional change in IVT is a reasonable approximation to the

thermodynamic contribution to IVT change. Thus, on top of concentrated warm coastal surface waters due to Gulf stream over western North Atlantic causing higher evaporation; specific humidity advecting from the tropics could be saturating the upper troposphere over the central north Atlantic and showing higher IVT300 and nIVT300.

Though AR mapping and characteristics study initially was started using IWV, the importance of tracking the AR made IVT as widely used method. However, using IWV would give estimation of concentration of total column condensable water vapour at a given instance (Ralph and Dettinger 2011; Gimeno et al., 2014). Climatology of IWV300 (IWV between 1000-300 hPa) (Figure 1c) and nIWV300 (nIWV between 1000-300 hPa) (Figure 1d) shows the gradient of water vapour varying from a maximum at equator and fading towards the pole. Using nIWV here shows the amount of total column condensable water vapour per degree Kelvin. The amount of evaporation caused by solar heating determines the extent and the scale of the water vapour. However, the occurrence of AR over a region and its magnitude guided by the amount of precipitable water vapour are not only bound to the availability of specific humidity in the atmosphere but also on the magnitude and direction of the winds carrying the water vapour. Hence, the higher intensity and magnitude of the ARs over the north Atlantic and western Europe are in the direct vicinity of the region of occurrence of extratropical cyclones (Pinto et al., 2013) and along the path of the subtropical westerly winds. Although all the methods used in mapping the ARs show higher values over the western North Atlantic, the origin of ARs and the region of moisture flux into the ARs in this part of the ocean are still debatable. These elongated features are also affected by the synoptic weather conditions, and their magnitude depends on the midway convergence of water vapour flux from adjacent areas. Despite IVT300 climatology showing a maximum of $300 \text{ kgm}^{-1}\text{s}^{-1}$, each AR could be different in magnitude and its strength varies as per the state of the atmosphere at a given instance.

AR intensity and bias in reanalysis data

Both accuracy and magnitude of atmospheric variables at different pressure levels (Q, U and V) in mapping ARs are highly dependent on the resolution of the data obtained. Many of the existing algorithms and mapping techniques are using atmospheric data from satellites and numerical models to study ARs. Numerical models have limitation in integrating the discretized version of the Navier-Stokes equations. Due to uncertainty in initial conditions, numerical approximation, and model deficiencies, the error increases nonlinearly and thus have decreasing forecast skill in simulating the state of the atmosphere with a good lead time (Lorenz, 1963). As the filament structures move with time, and the Eulerian method used to map the filaments make it hard to use observations. On the other hand, most of the ARs, originate from the large open oceans through both local evaporation and remote moisture flux convergence. Land-based stations could be handy in measuring the atmospheric parameters while the AR approach inland and landfall. Data obtained from both satellites and statistical methods have limitations in forecasting the landfall and intensity of ARs well in advance. In recent times machine learning techniques (Chapman et al., 2019; Kashinath et al., 2020) have evolved as other alternatives. However, the average error in estimating the intensity of ARs through IVT is around $40\text{-}60 \text{ kgm}^{-1}\text{s}^{-1}$ using different

sources of data including data from reanalysis and amounts to 22% of mean observed flux (Chapman et al., 2019, Lavers et al., 2018).

In the north Atlantic, different reanalysis products used to map the ARs show variability in magnitudes (Figure 3). The climatology (shaded) and standard deviation (contours) of ERA5 has lower IVT300 than any other reanalysis products used; while ERA-Interim has higher climatology and standard deviation. The highest standard deviation ($200 \text{ kgm}^{-1}\text{s}^{-1}$) is around 60% of the maximum values of climatology ($>300 \text{ kgm}^{-1}\text{s}^{-1}$) in all reanalysis datasets. Both climatology and standard deviation are high in JJA and low in MAM and has strong variability (Supplementary Figure 1a, 1b), similar pattern is seen for all analysis products. Although these values vary with seasons, both SON and DJF have longer stretch/extent of higher climatology and standard deviation values in the north Atlantic. Similarly, both these values have large spread and reaching western Europe in winter half-year (WHY) (ONDJFM) showing a high frequency of ARs during this time (Lavers et al., 2011, 2012). Low frequency in summer half-year (SHY) (AMJJAS) mainly concentrated over central Atlantic.

All reanalysis data sets are developed using numerical and statistical approaches integrated with observations with bias corrections. Thus, all these reanalysis datasets show a similar spatial pattern over the North Atlantic, but the difference in magnitudes could be attributed to the variability in the magnitudes of Q, U and V, which could be further due to bias in observations, discrepancies in product development. To illustrate it further, we compared the atmospheric parameters used (Q, U, and V) to map AR in 20CR (coarse resolution) with the ERA5 (high resolution data) (Figure S3). A simple interpolation has been used to match grids points of parameters in ERA5 with 20CR data as these data sets have a different spatial resolution. The climatology of these individual parameters during 1979-2014 shows that 20CR overestimating the magnitude (Figures S3d-S3f) compared to the ERA5 (Figures S3a-S3c). Hence, the 20CR data has a negative bias of 0.5 gKg^{-1} in Q, 1 ms^{-1} in U and V components of wind in the north Atlantic (Figures S3g-S3i). However, this would not be obvious for different seasons and different ARs in the Atlantic.

In the case of AR mapped on 6th March 2002, different reanalysis products show significant bias in IVT300 compared to ERA5 (Figure 4). Both MERRA and ERA-Interim show positive bias at the head of the AR (AR path is marked as the grey arrow in Figure 4) and negative bias in the tail (Figure 4a, 4b). On the other hand, NCEP (NCAR, CFS) and 20CR have a strong negative bias on aggregate (Figures 4c-4e). Both these positive and negative biases are around $50 \text{ kgm}^{-1}\text{s}^{-1}$ in magnitude and are of 10% of the total magnitude of AR ($\sim 500 \text{ kgm}^{-1}\text{s}^{-1}$) (Figure 2). The variability in the magnitude of IVT300 in different products might lead to bias in the intensity estimation of precipitation and winds during landfall. Hence, we use ERA5 data as a standard dataset in our further analysis in the following sections.

Spatio-temporal variability of IVT300

A general approach used to map the ARs is using IVT300 by considering pressure levels from surface (1000 hPa) to 300 hPa (Neiman et al., 2008b; Guan et al., 2010, Lavers et al., 2011). A few studies also

considered 900 hPa as the surface reference level (Gorodetskaya et al., 2014); 500 hPa (Yang et al., 2016) and 200 hPa (Sellars et al., 2017; Mattingly et al., 2018) as the upper limits. Shields et al., (2018) compiled all the available methods including thresholds to map ARs globally as a part of describing Atmospheric River Tracking Method Intercomparison Project (ARTMIP). Hence, there is persisting ambiguity in using reference pressure levels to map ARs. Therefore, here we quantify the magnitude of annual and semi-annual IVT in different layers. For this purpose, the total column (1000-300 hPa) has been divided into sublayers consisting 500-300 hPa (IVT_Upper), 750-300 hPa (IVT_Middle), 750-500 (IVT_Lower) which lie above 750 hPa pressure level in addition to computing IVT500 (1000-500 hPa) and IVT750 (1000-750 hPa). This exercise helps to map the strength of IVT and spatial variability in these layers which is a function of exponentially decreasing water vapour pressure with height.

The annual, WHY and SHY mean IVT computed using ERA5 data in IVT_Upper (Figures S4a, S4d, S4g), IVT_Middle (Figure S4b, S4e, S4h) and IVT_Lower (Figure S4c, S4f, S4i) are shown in Supplementary Figure S4. Due to low saturated water vapour in the higher altitudes, IVT_Upper in the north Atlantic has lower magnitude ($20 \text{ kgm}^{-1}\text{s}^{-1}$) as compared to IVT_Middle ($>80 \text{ kgm}^{-1}\text{s}^{-1}$) and IVT_Lower ($70 \text{ kgm}^{-1}\text{s}^{-1}$) during all seasons. Though the magnitude is less, the winds in the IVT_Upper plays a key role in guiding these narrow filaments of ARs. As the IVT_Middle (750-300 hPa) includes IVT_Upper (500-300 hPa), the resultant IVT in the 750-500 hPa layer is $60 \text{ kgm}^{-1}\text{s}^{-1}$. On segregating these pressure levels, IVT shows a dipole pattern with a low below 20°N over the northwestern African coast and a high in the central north Atlantic extending from 30°N to 60°N . The green rectangular box in Figure S4b shows the region with maximum IVT (30°N - 60°N , 80°W - 0). The magnitude of high in the dipole is further increased during SHY than other periods in all layers (Figure S4g-S4i). Similarly, the low has become further less during WHY (Figure S4d-S4f). Thus, IVT has maximum strength during SHY which could be due to increased evaporation over the warm waters in the North Atlantic. Figure 5 shows the strength of annual, SHY and WHY mean IVT in the central North Atlantic (30°N - 60°N , 80°W - 0) computed from ERA5 data using different reference pressure levels at the top (300 hPa, 500 hPa and 750 hPa) with respect to 1000 hPa. No significant difference was seen between IVT500 and IVT300 ($\sim 12 \text{ kgm}^{-1}\text{s}^{-1}$) during the study period. But, IVT750 contributing $\frac{3}{4}$ of the total strength of IVT300 and IVT500. Thus, the strength of the IVT300 and IVT500 depends on the near-surface processes below 750 hPa. While there were no large changes in the strength of the IVT in the individual layers with seasons; IVT in SHY has 3% higher magnitude, whereas IVT in WHY shows 3% lower magnitude compared to the annual mean (Figure 5). Hence, as the mean IVT is high up to 500 hPa irrespective of the season, and improved parameterization, in addition to accurate and high-resolution atmospheric data at least up to 500 hPa would be handy in better estimating the strength of the IVT in the north Atlantic.

Furthermore, we show hovmöller (Figure 6) of the monthly IVT300 in the central north Atlantic averaged between 30°N - 60°N along 80°W - 0 during 2014-2018 to study the seasonal variability of peak IVT300 in more detail. IVT300 peaks in the western Atlantic (along the east coast of North America) during summer months. Due to large temperature and pressure gradients from south to north coupled with extratropical cyclone season, high IVT300 has been shifting towards the eastern Atlantic in winter as marked with

arrows in Figure 6 and thus causing frequent ARs over western Europe during WHY. Yet, the extent, location and movement of the peak IVT300 were not constant and have large interannual variability with relatively low values during the spring season and hence the low AR activity during this time. This interannual and intraseasonal variability in IVT300 could be caused by the altering winds over this region. To study this further, we explored the decadal variability and trend in IVT300 and related atmospheric components in the following section.

IVT300 decadal variability and trend

It is evident that recent climate change during post-industrial era causing global warming and altering the global water cycle. On this note, it is important to look for the changes in the IVT variability and trend in the recent times due to warming surface and enhanced evaporation as the changing Clausius-Clapeyron scaling factor $\alpha(T)$ could increase the total water vapour content in the individual atmospheric layers. In Figure 7, we show the decadal trend and variability of IVT300 along with IVT of different layers of the atmosphere and its dependency on the variable atmospheric parameters using ERA5 data. For this purpose, we used the same box in the central North Atlantic (30°N-60°N, 80°W-0). Figure 7a shows an increasing annual trend of IVT300 (black line) in each decade over this region. Though the overall trend shows an increasing IVT300 over this region, the decadal trend has seesaw oscillations. An annual IVT300 trend ($1938 \text{ kgm}^{-1}\text{yr}^{-1}$) in the first decade i.e. 1979-1988 (red) is dominated by the annual trend in the second decade (green) with an increase of $3333 \text{ kgm}^{-1}\text{yr}^{-1}$ (1989-1998). Similarly, a large increase in the annual IVT300 in the recent decade (purple) with $5663 \text{ kgm}^{-1}\text{yr}^{-1}$ (2009-2018) dominates the previous decade (blue) with a moderate annual increase of $1783 \text{ kgm}^{-1}\text{yr}^{-1}$ (1999-2008).

This increasing annual IVT300 trend in each decade is in coherence with the increasing IVT below 750 hPa and IVT_Lower (750-500 hPa) (Figure 7b). Particularly IVT750 has contributed more to the large increase in second (1988-1998) and fourth decades (2009-2018). As the IVT is proportional to Q, U and V; the changes in these parameters would impact these trends. Thus, the large trend of IVT300 in the second decade is dominated by the availability of Q in the near-surface layer (1000-750 hPa) which has an annual increasing trend of 2.5 gkg^{-1} and is largest in all decades (Figure 7c). However, the negative trend in the zonal and meridional components of wind (Figures 7d, 7e) in all layers during the same time, guiding the total trend in the second decade. Though Q has a positive trend in the first and third decades, the negative trend in wind components in different layers caused the IVT annual trend to be moderate in these decades. On the other hand, the annual trend of both Q and wind components (U and V) were positive in the fourth decade (Figure 7c-7e) and thus led to a strong increase in the annual IVT300 in all layers (Figure 7b).

The spatial trend analysis significant at 95% during annual, WHY and SHY using daily IVT300 data from ERA5 is shown in Figure 8. While the annual trend shows a rapid increase ($3000 \text{ kgm}^{-1}\text{yr}^{-1}$) of IVT300 at 20°N in the Atlantic and along the western Atlantic extended into central Atlantic with mean annual IVT300 increase of $2000 \text{ kgm}^{-1}\text{yr}^{-1}$, there was no significant increase in IVT300 over southwestern Europe

during the study period (Figure 8c). Both WHY and SHY show opposite spatial trends. IVT300 was increased in the central Atlantic and the southwestern United Kingdom during SHY, which could be triggered by the large IVT300 available over the western Atlantic during this time (Figure 8b, Figure 6). Though the WHY show the opposite patterns with a negative trend in IVT300, the low is in the northern United Kingdom. There was a moderate increase in the IVT300 trend along southwestern Europe and the region below 20°N has large positive trend during WHY (Figure 8a). IVT300 has been increasing poleward in the recent times with a strong positive trend along 45°W during all the seasons, which could further guide intense AR towards the north.

Categories and frequency of ARs over the north Atlantic

Furthermore, we study the spatial variability of frequency of ARs over North Atlantic using different categories of IVT300 as shown in table 3. We distinguish the daily IVT300 based on the magnitude of the intensity at each grid point or location in the selected region without consciousness on the duration of the event. The spatial frequency has been computed using the percentage of the ratio of the number of days of IVT300 of a category to the total number of days in the study period (14610). Thus, the cat 1 events are more frequent in the north Atlantic which occurs at 50% of the time (Figure 9a) along the southwest coast of Europe and in the central Atlantic. Other categories such as cat 2 (Figure 9b), cat 3 (Figure 9c) and cat 4 (Figure 9d) are less frequent (<15%) over the Euro-Atlantic sky. The source of this intense IVT300 is along the western Atlantic and a few events are reaching the west coast of Europe. Thus, the frequency of the intense ARs over Europe is less with cat 2 IVT300 being at 8%, cat 3 and cat 4 are at below 1% of the time. Nonetheless, the rare intense events which occur at less than 1% of the time could cause large damage over land when they come inland. To investigate the same along western Europe, we draw the frequency histogram (Figure 10a) and compute the probability density function (Figure 10b) along 11°W as a gateway to western Europe. This is a contrary to Lavers et al., (2013) who considered 10°W as the reference longitude which intersects with some parts of the land over the United Kingdom. Assuming 11°W and 35°N-70°N would eliminate the IVT300 interaction with land.

Table 3: Categories of IVT300 based on intensity

S. No	Category	Threshold ($\text{kgm}^{-1}\text{s}^{-1}$)
1	Cat1	$200 \leq \text{IVT300} < 500$
2	Cat2	$500 \leq \text{IVT300} < 750$
3	Cat3	$750 \leq \text{IVT300} < 1000$
4	Cat4	$\text{IVT300} \leq 1000$

While most of the IVT300 values along the west coast during the study period are below $300 \text{ kgm}^{-1}\text{s}^{-1}$ (Figure 10a), the values reaching $800 \text{ kgm}^{-1}\text{s}^{-1}$ in a few instances could lead to extreme ARs. Similarly, the

probability density function computed along the same boundary (Figure 10b) shows the IVT300 could reach up to $1400 \text{ kgm}^{-1}\text{s}^{-1}$ and cat 1 IVT300 has the higher probability of occurrence (0.06) over western Europe than other categories. The decadal analysis along the same longitude (Figure 11) shows an increasing extreme IVT300 values and their poleward shift in recent decades. All categories show peak frequency between 40°N - 60°N and there was no explicit decadal variability of cat 1 IVT300 along 11°W (Figure 11a). But cat 2 (Figure 11b,11c) shows low frequency during the first (black) and third decades between 40°N - 60°N (green). On the other hand, the frequency of cat 3 and cat 4 IVT300 has been increasing with time (Figure 11d) and there is poleward movement crossing 60°N . The changes in the atmospheric state and the synoptic condition in recent decades could be causing the poleward movement of the intense IVT300. Hence, in the following section, we study the state of the atmosphere during the occurrence of IVT300 over western Europe.

Atmospheric state and synoptic conditions

The Euro-Scandinavian blocking including phases of the North Atlantic Oscillation (NAO) dominates the weather patterns over Europe and Scandinavia through the impact on precipitation and temperature (Madonna et al., 2017). While these patterns are persistent in the North Atlantic-European sector irrespective of the seasons, mostly these patterns control the wintertime weather regimes (Dawson et al., 2012; Hannachi et al., 2017). On the other hand, western Europe receives frequent intense IVT300 (ARs) in wintertime than in any other season. To study the atmospheric and synoptic conditions while IVT300 occurrence and landfalling along western Europe, we study the composite of 500 hPa geopotential (GP) (Figure 12) and surface latent heat flux (SLHF) (Figure 13) anomalies following Lavers et al., (2013) along 11°W using 5° latitude bins spanning 35°N - 70°N . Contrary to Lavers et al. (2013), who used only 10 intense ARs, we computed GP and SLHF anomaly composites with all instances (days) where IVT300 greater than $200 \text{ kgm}^{-1}\text{s}^{-1}$ in these latitude bins. Initially, we computed these daily GP and SLHF anomalies with respect to same time (day) period over the years 1979-2018. Then, these anomalies were picked with respect to time and location of the occurrence of IVT300 greater than $200 \text{ kgm}^{-1}\text{s}^{-1}$ within the selected bins and the composite mean anomaly was calculated for each latitude bin.

GP shows a tripole pattern with positive anomalies over south of Iberian Peninsula (Figure 12a and 12b); Iceland and Greenland, and negative anomalies extend from Britain to the Iberian Peninsula. This is also termed as an Atlantic ridge regime with blocking mainly offshore of the Iberian Peninsula due to Iberian wave breaking (Davini et al., 2014) or southwest European blocking (Woollings et al., 2010) leading to the southward occurring ARs (35°N - 45°N). The Greenland anticyclone regime occurs mainly over Greenland resembling the negative phase of the NAO. This negative NAO arrangement would block the flow over northern Europe and the North Atlantic storm track and related heavy precipitation and thus impacts southern Europe (Pinto and Raible, 2012). The zonal regime with very little blocking resembling the positive phase of the NAO. In a positive NAO phase, negative GP anomalies (Figure 12c and 12d) in the 45°N - 55°N latitude band favors occurrence of frequent IVT300 within the extratropical cyclones causing rainfall over northern France, through the western British Isles to Norway. A Scandinavian blocking regime

is associated with blocking mainly over the European continent and Scandinavia. The occurrence of IVT300 (ARs) and their associated precipitation in the north between 55°N-70°N is related to Scandinavian blocking with the dipole of positive anomalies near the British Isles and negative anomalies over Greenland and Iceland (Figure 12e-12g). Although both NAO and Scandinavian patterns have strong relation with IVT300 occurrence in Europe, it is not obvious that each IVT300 (AR) landfall would follow the same synoptic weather patterns as the spatial pattern of the atmospheric state would vary significantly with time over a region.

Southernmost IVT300 events are drawing water vapour from both western and eastern North Atlantic as the SLHF anomalies show a dipole pattern with positive anomalies on either side (Figure 13a, 13b). Thus, these regions act as source to moisture entraining into ARs and impact the intensity of IVT300. The north-central Atlantic is the source of moisture for the IVT300 in the 45°N-55°N latitude band (Figure 13c, 13d). Further, a dipole pattern with positive SLHF anomaly in the west and negative in the east fueling IVT300 in the far north. Though the positive anomalies over the North Atlantic could lead to intensifying IVT300 in the north, the cold sea surface and associated negative SLHF anomalies over the Scandinavia could control the total moisture flux into the IVT300 and hence the intensity of ARs over this region.

Conclusions

We study the spatio-temporal variability of water vapour transport as a proxy to ARs in the Euro-Atlantic sky using six-hourly data from six reanalysis data sets available from NOAA, NASA, ECMWF and NCEP during 1979-2018. We use IVT and IWV methods to map the water vapour transport in different atmospheric layers the North Atlantic and normalized with temperature to study the water vapour variability with temperature. Both IVT and nIVT proved to accurate enough to map ARs. Though the IVT shows seasonal and semi-annual variability; the mean annual climatology of IVT300 is $300 \text{ kgm}^{-1}\text{s}^{-1}$, and the standard deviation is at 60% of the climatology in the north Atlantic. On the other hand, both these values vary in different reanalysis products with recently released ERA5 showing lower climatology and standard deviation whereas ERA-Interim has higher values compared to other reanalysis datasets. However, the average bias in other datasets is around $60 \text{ kgm}^{-1}\text{s}^{-1}$ as compared to ERA5 which amounts to 22% of the total observed flux. The bias in the magnitude of IVT in different layers is directly proportional to the bias in the Q, U and V of respective layers.

While most of the water vapour flux located below 500 hPa due to rapidly decreasing saturated moisture flux with height, the upper layer winds are key to transport the flux poleward. Hence, the accurate and high-resolution atmospheric parameters at least up to 500 hPa could improve the detection and tracking of ARs in the north Atlantic. On the other hand, the variability and trend of Q, U and V below 750 hPa guide the strength of the total column IVT. Thus, Q, U, and V below 750 hPa control the magnitude of IVT in the north Atlantic which shows an increasing decadal trend with seesaw decadal variability. The IVT in the north Atlantic shows interannual variability with the zonal movement of peak values from the western Atlantic in summer to the eastern Atlantic in winter. However, the strength of the IVT in the Atlantic is 3% higher in summer as compared to annual mean due to strong evaporation from the warm ocean than 3%

low in winter. While the semi-annual spatial trend of IVT300 shows an opposite pattern, the annual trend of IVT300 shows an increasing water vapour flux over western Atlantic with a poleward movement of this flux. Thus, the higher latitudes encountering intense ARs in recent times. Though the category 1 IVT300 are more frequent (50%) in the North Atlantic, particularly over 40°N-60°N, the rarely occurring (15%) higher category events could cause extreme precipitation, flooding and winds over western Europe. The atmospheric state and synoptic weather guided by Scandinavian blocking and both phases of NAO set the landfall location of the ARs along western Europe.

Declarations

Acknowledgement

Authors thank NOAA Earth System Research Laboratories (ESRL), the European Centre for Medium-Range Weather Forecasts (ECMWF), National Aeronautics and Space Administration (NASA), and the National Centers for Environmental Prediction (NCEP) for providing reanalysis datasets. We acknowledge Pyferret software from the NOAA/PMEL. We acknowledge the Department of Earth Sciences, Uppsala University and The Swedish Research Council (VR), Sweden for supporting this study.

Data availability

All the data used in the study are freely available online from the corresponding data sources cited in the article. However, the data that support the findings of this study are available on request from the corresponding author.

Code availability

All codes used in this study are available on request from the corresponding author.

Author contributions

V.T. conceived the research plan, performed data analysis, and prepared the first draft, A.R. and E.S helped to improve the research plan and figures, and contributed to analyze the results. All authors contributed to write and review the paper.

References

1. Blamey, R. C., A. M. Ramos, R. M. Trigo, R. Tomé, and C. J. C. Reason. "The influence of atmospheric rivers over the South Atlantic on winter rainfall in South Africa." *Journal of Hydrometeorology* 19, no. 1 (2018): 127-142.
2. Champion, Adrian J., Richard P. Allan, and David A. Lavers. "Atmospheric rivers do not explain UK summer extreme rainfall." *Journal of Geophysical Research: Atmospheres* 120, no. 14 (2015): 6731-6741.

3. Chapman, W. E., A. C. Subramanian, L. Delle Monache, S. P. Xie, and F. M. Ralph. "Improving Atmospheric River Forecasts With Machine Learning." *Geophysical Research Letters* 46, no. 17-18 (2019): 10627-10635.
4. Cheng, Brian S., Andrew L. Chang, Anna Deck, and Matthew C. Ferner. "Atmospheric rivers and the mass mortality of wild oysters: insight into an extreme future?." *Proceedings of the Royal Society B: Biological Sciences* 283, no. 1844 (2016): 20161462.
5. Compo, G.P., J.S. Whitaker, P.D. Sardeshmukh, N. Matsui, R.J. Allan, X. Yin, B.E. Gleason, R.S. Vose, G. Rutledge, P. Bessemoulin, S. Brönnimann, M. Brunet, R.I. Crouthamel, A.N. Grant, P.Y. Groisman, P.D. Jones, M. Kruk, A.C. Kruger, G.J. Marshall, M. Maugeri, H.Y. Mok, Ø. Nordli, T.F. Ross, R.M. Trigo, X.L. Wang, S.D. Woodruff, and S.J. Worley, 2011: The Twentieth Century Reanalysis Project. *Quarterly J. Roy. Meteorol. Soc.*, 137, 1-28. <http://dx.doi.org/10.1002/qj.776>
6. Cordeira, Jason M., Jonathan Stock, Michael D. Dettinger, Allison M. Young, Julie F. Kalansky, and F. Martin Ralph. "A 142-year climatology of northern California landslides and atmospheric rivers." *Bulletin of the American Meteorological Society* 100, no. 8 (2019): 1499-1509.
7. Dawson A, Palmer TN, Corti S. 2012. Simulating regime structures in weather and climate prediction models. *Geophys. Res. Lett.* 39: L21805.
8. Dee, D. P., and 35 co-authors, 2011: The ERA-Interim reanalysis: Configuration and performance of the data assimilation system. *Quart. J. R. Meteorol. Soc.*, 137, 553-597. DOI: 10.1002/qj.828.
9. Dettinger, M. (2011). Climate change, atmospheric rivers, and floods in California—a multimodel analysis of storm frequency and magnitude changes 1. *JAWRA Journal of the American Water Resources Association*, 47(3), 514-523.
10. Dettinger, M. D., F. M. Ralph, T. Das, P. J. Neiman, and D. R. Cayan (2011), Atmospheric rivers, floods and the water resources of California, *Water*, 3, 445–478, doi:10.3390/w3020445.
11. Dettinger, Michael D., Fred Martin Ralph, Tapash Das, Paul J. Neiman, and Daniel R. Cayan. "Atmospheric rivers, floods and the water resources of California." *Water* 3, no. 2 (2011): 445-478.
12. Fish, Meredith A., Anna M. Wilson, and F. Martin Ralph. "Atmospheric River Families: Definition and Associated Synoptic Conditions." *Journal of Hydrometeorology* 20, no. 10 (2019): 2091-2108.
13. Florsheim, Joan L., and Michael D. Dettinger. "Promoting atmospheric-river and snowmelt-fueled biogeomorphic processes by restoring river-floodplain connectivity in California's Central Valley." In *Geomorphic approaches to integrated floodplain management of lowland fluvial systems in North America and Europe*, pp. 119-141. Springer, New York, NY, 2015.
14. Gao, Yang, Jian Lu, and L. Ruby Leung. "Uncertainties in projecting future changes in atmospheric rivers and their impacts on heavy precipitation over Europe." *Journal of Climate* 29, no. 18 (2016): 6711-6726.
15. Gao, Yang, Jian Lu, and L. Ruby Leung. "Uncertainties in projecting future changes in atmospheric rivers and their impacts on heavy precipitation over Europe." *Journal of Climate* 29, no. 18 (2016): 6711-6726.

16. Gelaro, Ronald, Will McCarty, Max J. Suárez, Ricardo Todling, Andrea Molod, Lawrence Takacs, Cynthia A. Randles et al. "The modern-era retrospective analysis for research and applications, version 2 (MERRA-2)." *Journal of Climate* 30, no. 14 (2017): 5419-5454.
17. Gimeno, Luis, Andreas Stohl, Ricardo M. Trigo, Francina Dominguez, Kei Yoshimura, Lisan Yu, Anita Drumond, Ana María Durán-Quesada, and Raquel Nieto. "Oceanic and terrestrial sources of continental precipitation." *Reviews of Geophysics* 50, no. 4 (2012).
18. Gimeno, Luis, Raquel Nieto, Marta Vázquez, and David A. Lavers. "Atmospheric rivers: A mini-review." *Frontiers in Earth Science* 2 (2014).
19. Gimeno, Luis. "Grand challenges in atmospheric science." *Frontiers in Earth Science* 1 (2013).
20. Gonzales, K. R., Swain, D. L., Nardi, K. M., Barnes, E. A., & Diffenbaugh, N. S. (2019). Recent warming of landfalling atmospheric rivers along the west coast of the United States. *Journal of Geophysical Research: Atmospheres*, 124(13), 6810-6826.
21. Gorodetskaya, Irina V., Maria Tsukernik, Kim Claes, Martin F. Ralph, William D. Neff, and Nicole PM Van Lipzig. "The role of atmospheric rivers in anomalous snow accumulation in East Antarctica." *Geophysical Research Letters* 41, no. 17 (2014): 6199-6206.
22. Guan, Bin, and Duane E. Waliser. "Atmospheric rivers in 20 year weather and climate simulations: A multimodel, global evaluation." *Journal of Geophysical Research: Atmospheres* 122, no. 11 (2017): 5556-5581.
23. Guan, Bin, and Duane E. Waliser. "Detection of atmospheric rivers: Evaluation and application of an algorithm for global studies." *Journal of Geophysical Research: Atmospheres* 120, no. 24 (2015): 12514-12535.
24. Guan, Bin, Noah P. Molotch, Duane E. Waliser, Eric J. Fetzer, and Paul J. Neiman. "Extreme snowfall events linked to atmospheric rivers and surface air temperature via satellite measurements." *Geophysical Research Letters* 37, no. 20 (2010).
25. Hack, James J., Julie M. Caron, Stephen G. Yeager, Keith W. Oleson, Marika M. Holland, John E. Truesdale, and Philip J. Rasch. "Simulation of the global hydrological cycle in the CCSM Community Atmosphere Model version 3 (CAM3): Mean features." *Journal of climate* 19, no. 11 (2006): 2199-2221.
26. Hannachi A, Straus DM, Franzke CLE, Corti S, Woollings T. 2017. Low-frequency nonlinearity and regime behavior in the Northern Hemisphere extratropical atmosphere. *Rev. Geophys.* 55: 199-234.
27. Hersbach, H et al., Copernicus Climate Change Service (C3S) (2017): ERA5: Fifth generation of ECMWF atmospheric reanalyses of the global climate. Copernicus Climate Change Service Climate Data Store (CDS)
28. Huning, Laurie S., Steven A. Margulis, Bin Guan, Duane E. Waliser, and Paul J. Neiman. "Implications of detection methods on characterizing atmospheric river contribution to seasonal snowfall across Sierra Nevada, USA." *Geophysical Research Letters* 44, no. 20 (2017): 10-445.

29. Kamae, Youichi, Wei Mei, and Shang-Ping Xie. "Climatological relationship between warm season atmospheric rivers and heavy rainfall over East Asia." *Journal of the Meteorological Society of Japan. Ser. II* (2017).
30. Kanamitsu, Masao, Wesley Ebisuzaki, Jack Woollen, Shi-Keng Yang, J. J. Hnilo, M. Fiorino, and G. L. Potter. "Ncep–doe amip-ii reanalysis (r-2)." *Bulletin of the American Meteorological Society* 83, no. 11 (2002): 1631-1644.
31. Kashinath, K., Mudigonda, M., Kim, S., Kapp-Schwoerer, L., Graubner, A., Karaismailoglu, E., ... & Lewis, C. (2020). ClimateNet: an expert-labelled open dataset and Deep Learning architecture for enabling high-precision analyses of extreme weather. *Geoscientific Model Development Discussions*, 1-28.
32. Kaye L. Brubaker, Dara Entekhabi, and Peter S. Eagleson. Atmospheric water vapor transport and continental hydrology over the Americas. Technical Report 3-4, 1994.
33. Khouakhi, A., and G. Villarini. "On the relationship between atmospheric rivers and high sea water levels along the US West Coast." *Geophysical Research Letters* 43, no. 16 (2016): 8815-8822.
34. Komatsu, Kensuke K., Vladimir A. Alexeev, Irina A. Repina, and Yoshihiro Tachibana. "Poleward upgliding Siberian atmospheric rivers over sea ice heat up Arctic upper air." *Scientific reports* 8, no. 1 (2018): 1-15.
35. Kundzewicz, Zbigniew W., Maciej Radziejewski, and Iwona Pinskiwar. "Precipitation extremes in the changing climate of Europe." *Climate Research* 31, no. 1 (2006): 51-58.
36. Lavers, David A., and Gabriele Villarini. "The contribution of atmospheric rivers to precipitation in Europe and the United States." *Journal of Hydrology* 522 (2015): 382-390.
37. Lavers, David A., Florian Pappenberger, David S. Richardson, and Ervin Zsoter. "ECMWF Extreme Forecast Index for water vapor transport: A forecast tool for atmospheric rivers and extreme precipitation." *Geophysical Research Letters* 43, no. 22 (2016): 11-852.
38. Lavers, David A., Gabriele Villarini, Richard P. Allan, Eric F. Wood, and Andrew J. Wade. "The detection of atmospheric rivers in atmospheric reanalyses and their links to British winter floods and the large-scale climatic circulation." *Journal of Geophysical Research: Atmospheres* 117, no. D20 (2012).
39. Lavers, David A., Mark J. Rodwell, David S. Richardson, F. Martin Ralph, James D. Doyle, Carolyn A. Reynolds, Vijay Tallapragada, and Florian Pappenberger. "The gauging and modeling of rivers in the sky." *Geophysical Research Letters* 45, no. 15 (2018): 7828-7834.
40. Lavers, David A., Richard P. Allan, Eric F. Wood, Gabriele Villarini, David J. Brayshaw, and Andrew J. Wade. "Winter floods in Britain are connected to atmospheric rivers." *Geophysical Research Letters* 38, no. 23 (2011).
41. Lavers, David A., Richard P. Allan, Eric F. Wood, Gabriele Villarini, David J. Brayshaw, and Andrew J. Wade. "Winter floods in Britain are connected to atmospheric rivers." *Geophysical Research Letters* 38, no. 23 (2011).
42. Leung, L. Ruby, and Yun Qian. "Atmospheric rivers induced heavy precipitation and flooding in the western US simulated by the WRF regional climate model." *Geophysical Research Letters* 36, no. 3

(2009).

43. Madonna, E., Li, C., Grams, C. M., & Woollings, T. (2017). The link between eddy-driven jet variability and weather regimes in the North Atlantic-European sector. *Quarterly Journal of the Royal Meteorological Society*, 143(708), 2960-2972.
44. Mattingly, K. S., T. L. Mote, and Xavier Fettweis. "Atmospheric river impacts on Greenland Ice Sheet surface mass balance." *Journal of Geophysical Research: Atmospheres* 123, no. 16 (2018): 8538-8560.
45. Millán, Millán M. "Extreme hydrometeorological events and climate change predictions in Europe." *Journal of Hydrology* 518 (2014): 206-224.
46. Nash, Deanna, Duane Waliser, Bin Guan, Hengchun Ye, and F. Martin Ralph. "The role of atmospheric rivers in extratropical and polar hydroclimate." *Journal of Geophysical Research: Atmospheres* 123, no. 13 (2018): 6804-6821.
47. Neff, William. "Atmospheric rivers melt Greenland." *Nature Climate Change* 8, no. 10 (2018): 857-858.
48. Neiman, Paul J., F. Martin Ralph, Gary A. Wick, Jessica D. Lundquist, and Michael D. Dettinger. "Meteorological characteristics and overland precipitation impacts of atmospheric rivers affecting the West Coast of North America based on eight years of SSM/I satellite observations." *Journal of Hydrometeorology* 9, no. 1 (2008): 22-47.
49. Neiman, Paul J., Lawrence J. Schick, F. Martin Ralph, Mimi Hughes, and Gary A. Wick. "Flooding in western Washington: The connection to atmospheric rivers." *Journal of Hydrometeorology* 12, no. 6 (2011): 1337-1358.
50. Pasquier, J. T., Stephan Pfahl, and Christian M. Grams. "Modulation of atmospheric river occurrence and associated precipitation extremes in the North Atlantic Region by European weather regimes." *Geophysical Research Letters* 46, no. 2 (2019): 1014-1023.
51. Payne, Ashley E., Marie-Estelle Demory, L. Ruby Leung, Alexandre M. Ramos, Christine A. Shields, Jonathan J. Rutz, Nicholas Siler, Gabriele Villarini, Alex Hall, and F. Martin Ralph. "Responses and impacts of atmospheric rivers to climate change." *Nature Reviews Earth & Environment* (2020): 1-15.
52. Pinto, J. G., and C. C. Raible (2012), Past and recent changes in the North Atlantic oscillation, *WIREs Clim. Change*, 3,79–90, doi:10.1002/wcc.150.
53. Pinto, Joaquim G., Nina Bellenbaum, Melanie K. Karremann, and Paul M. Della-Marta. "Serial clustering of extratropical cyclones over the North Atlantic and Europe under recent and future climate conditions." *Journal of geophysical research: Atmospheres* 118, no. 22 (2013): 12-476.
54. Ralph, F. M., & Dettinger, M. D. (2011). Storms, floods, and the science of atmospheric rivers. *Eos, Transactions American Geophysical Union*, 92(32), 265-266.
55. Ralph, F. Martin, Jonathan J. Rutz, Jason M. Cordeira, Michael Dettinger, Michael Anderson, David Reynolds, Lawrence J. Schick, and Chris Smallcomb. "A scale to characterize the strength and impacts of atmospheric rivers." *Bulletin of the American Meteorological Society* 100, no. 2 (2019): 269-289.

56. Ramos, Alexandre M., Ross C. Blamey, Iago Algarra, Raquel Nieto, Luis Gimeno, Ricardo Tomé, Chris JC Reason, and Ricardo M. Trigo. "From Amazonia to southern Africa: atmospheric moisture transport through low level jets and atmospheric rivers." *Ann. NY Acad. Sci* 1436 (2018): 217-230.
57. Saha, Suranjana, Shrinivas Moorthi, Xingren Wu, Jiande Wang, Sudhir Nadiga, Patrick Tripp, David Behringer et al. "The NCEP climate forecast system version 2." *Journal of climate* 27, no. 6 (2014): 2185-2208.
58. Schneider, Edwin K., Ben P. Kirtman, and Richard S. Lindzen. "Tropospheric water vapor and climate sensitivity." *Journal of the atmospheric sciences* 56, no. 11 (1999): 1649-1658.
59. Thapa, Kritika, Theodore A. Endreny, and Craig R. Ferguson. "Atmospheric rivers carry nonmonsoon extreme precipitation into Nepal." *Journal of Geophysical Research: Atmospheres* 123, no. 11 (2018): 5901-5912.
60. Thapa, Kritika, Theodore A. Endreny, and Craig R. Ferguson. "Atmospheric rivers carry non monsoon extreme precipitation into Nepal." *Journal of Geophysical Research: Atmospheres* 123, no. 11 (2018): 5901-5912.
61. Trenberth, Kevin E. "Changes in precipitation with climate change." *Climate Research* 47, no. 1-2 (2011): 123-138.
62. Van den Besselaar, E. J. M., A. M. G. Klein Tank, and T. A. Buishand. "Trends in European precipitation extremes over 1951–2010." *International Journal of Climatology* 33, no. 12 (2013): 2682-2689.
63. Waliser, Duane, and Bin Guan. "Extreme winds and precipitation during landfall of atmospheric rivers." *Nature Geoscience* 10, no. 3 (2017): 179-183.
64. Yang, Yan, Tongtiegang Zhao, Guangheng Ni, and Ting Sun. "Atmospheric rivers over the Bay of Bengal lead to northern Indian extreme rainfall." *International Journal of Climatology* 38, no. 2 (2018): 1010-1021.
65. Yang, Yan, Tongtiegang Zhao, Guangheng Ni, and Ting Sun. "Atmospheric rivers over the Bay of Bengal lead to northern Indian extreme rainfall." *International Journal of Climatology* 38, no. 2 (2018): 1010-1021.
66. Zhu, Yong, and Reginald E. Newell. "A proposed algorithm for moisture fluxes from atmospheric rivers." *Monthly weather review* 126, no. 3 (1998): 725-735.
67. Zhu, Yong, and Reginald E. Newell. "A proposed algorithm for moisture fluxes from atmospheric rivers." *Monthly weather review* 126, no. 3 (1998): 725-735.
68. Zhu, Yong, and Reginald E. Newell. "Atmospheric rivers and bombs." *Geophysical Research Letters* 21, no. 18 (1994): 1999-2002.

Figures

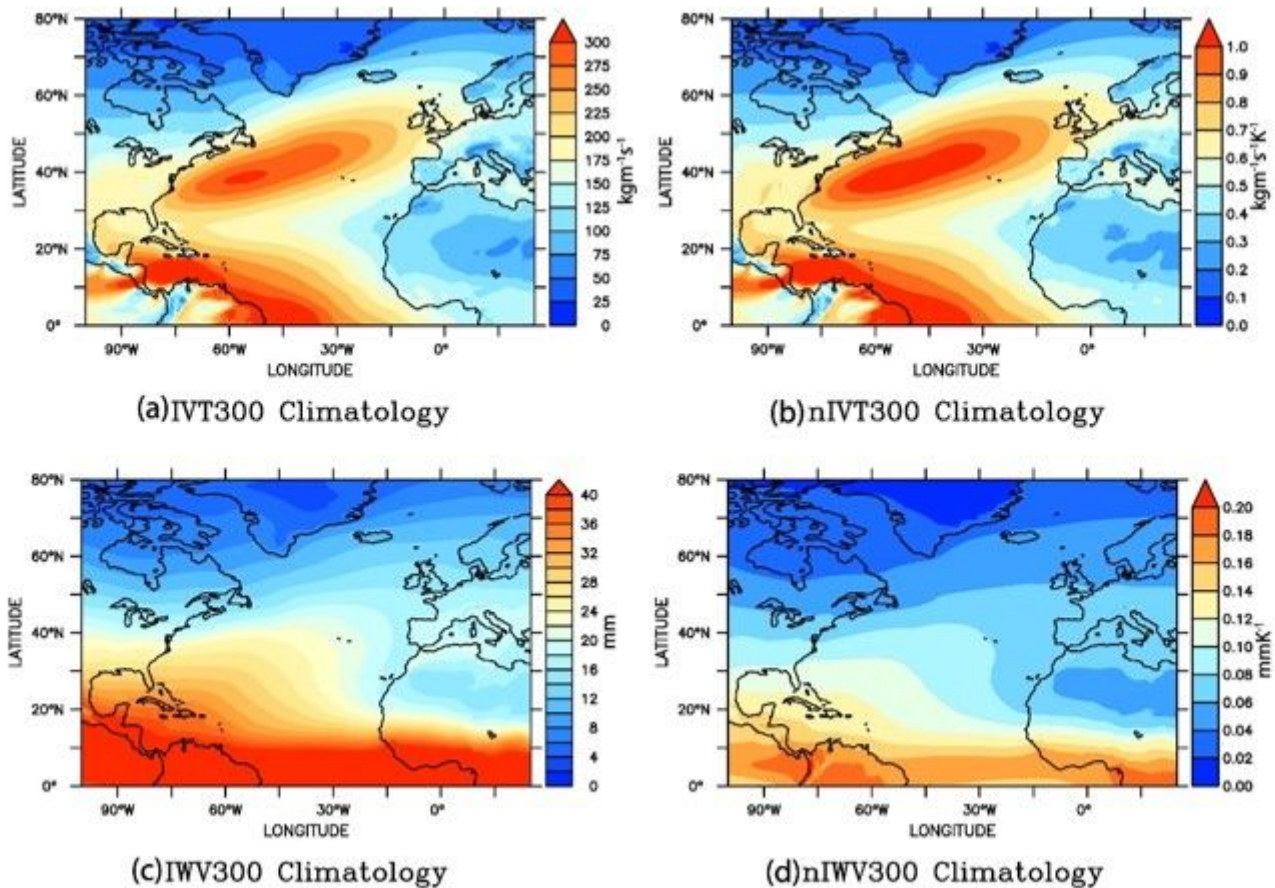


Figure 1

Climatology of ARs computed from daily ERA5 data using four different methods in the north Atlantic. One example of an AR from 6th March 2002 mapped using four different methods in Figure 2 has IVT300 higher than $500 \text{ kgm}^{-1}\text{s}^{-1}$ (Figure 2a). This event was one of the intense ARs occurred over northern Europe and caused excess rainfall over Britain and southern Scandinavia. While the IVT300 is narrow and short, nIVT300 (Figure 2b) shows the adjacent regions saturated with water vapour. The advected moisture from these surrounding regions could enhance the intensity and lifetime of the AR over a given location. Thus, nIVT300 is a useful method in mapping the true characteristics and saturated water vapour content in AR. Similarly, IWV300 and nIWV300 (Figures 2c, 2d) for this event show origin of AR and the source of the advection, which is, in this case, occurred from the warm tropical region (20°N) enriched with high specific humidity.

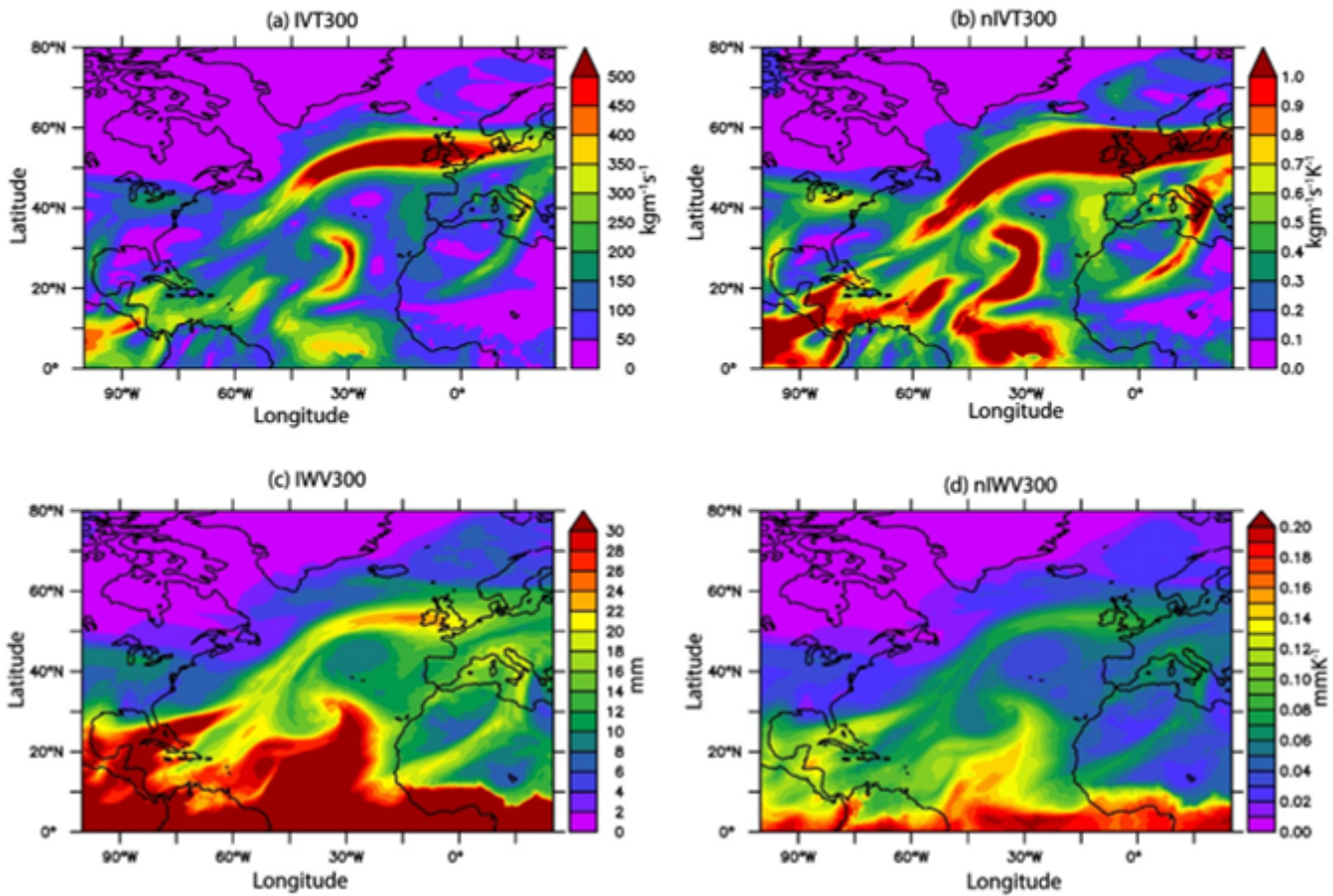


Figure 2

AR event on 2002 March 06 mapped using four different methods in the north Atlantic using ERA5 data.

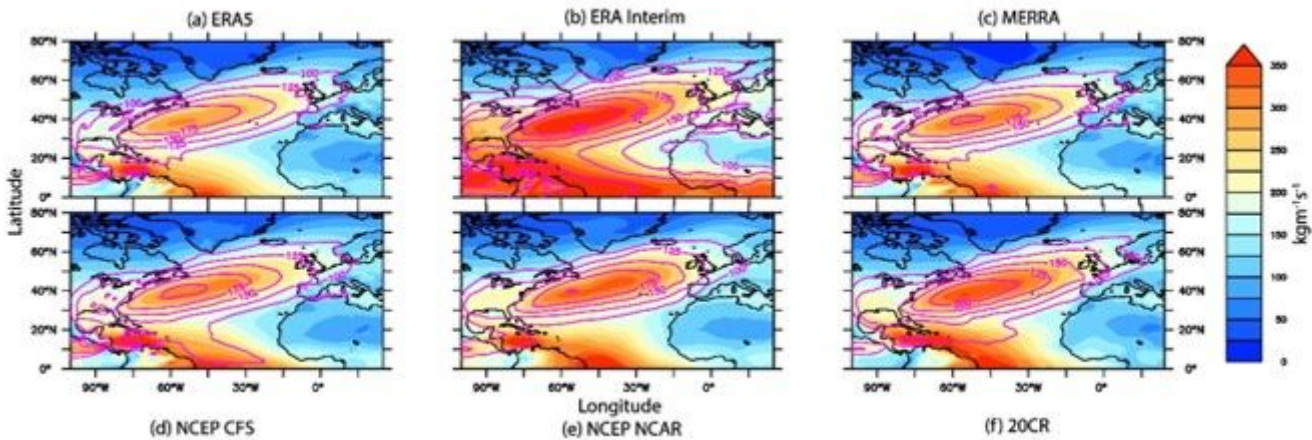


Figure 3

Climatology and standard deviation of IVT300 in the north Atlantic from all reanalysis data used in the study

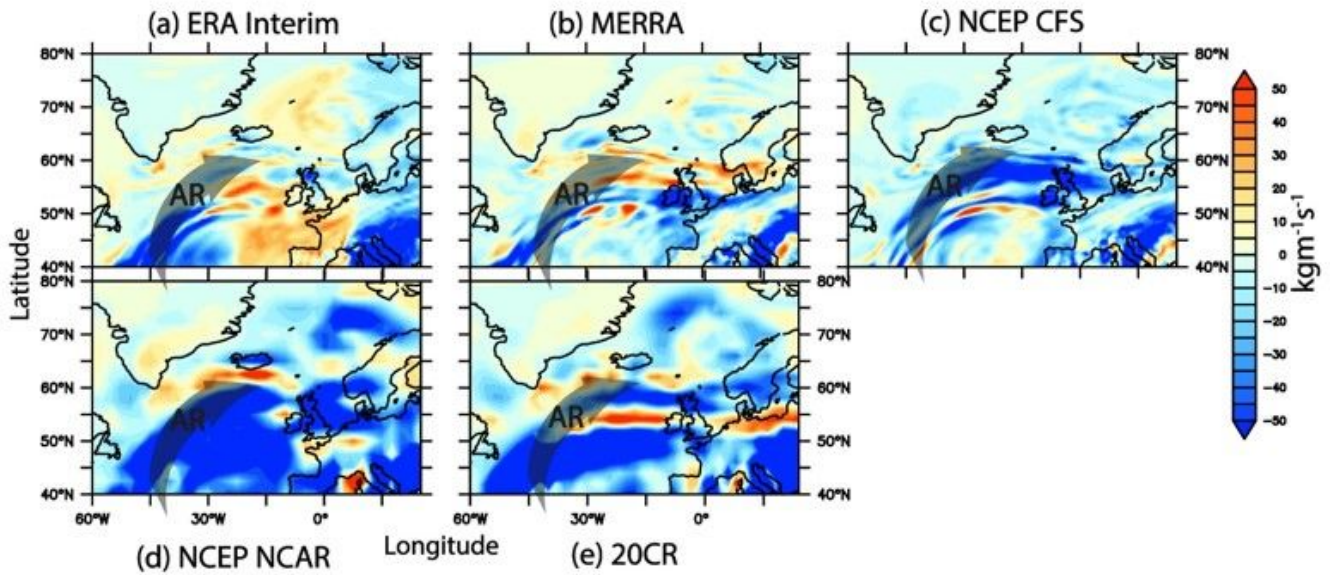


Figure 4

Bias in reanalysis products compared to ERA5 data in mapping AR on 2002 March 06 using IVT300 algorithm.

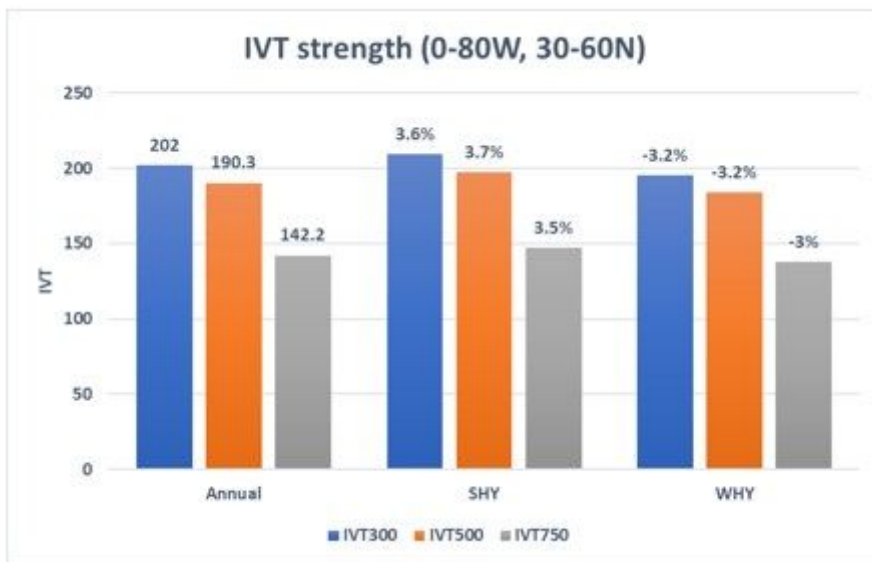


Figure 5

Strength of annual, SHY and WHY mean IVT in different layers

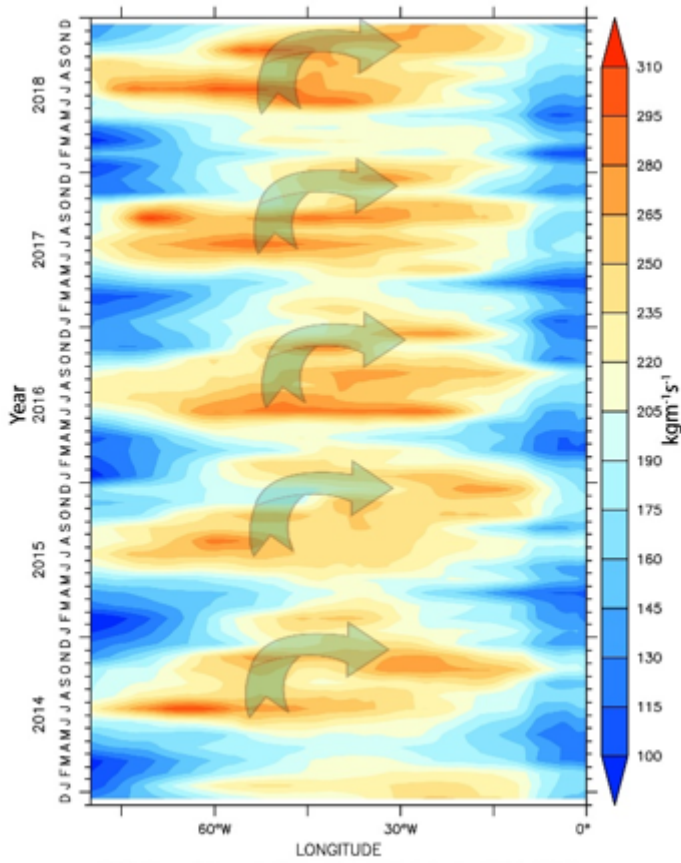


Figure 6

Strength of annual, SHY and WHY mean IVT in different layers

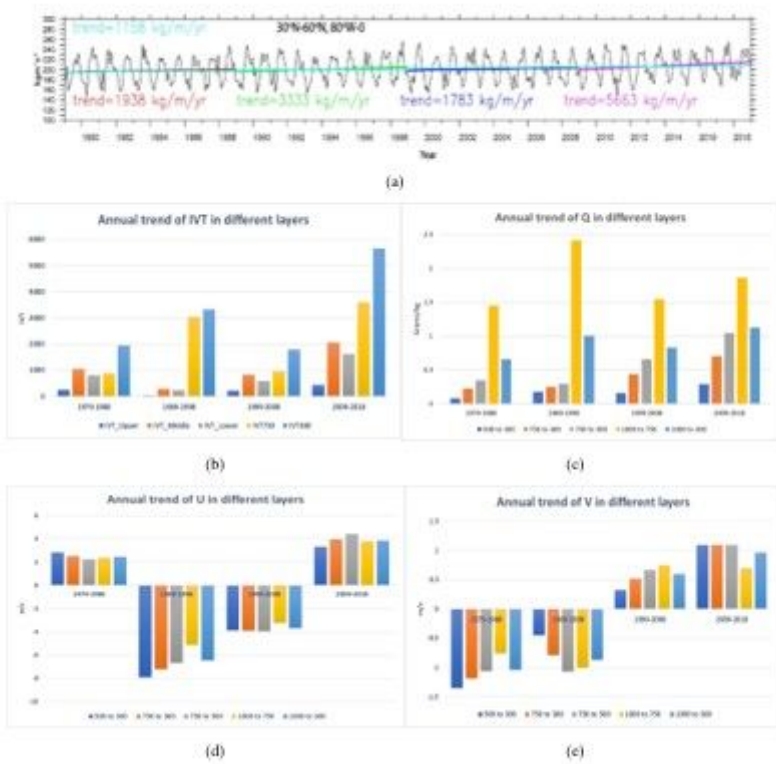


Figure 7

Decadal trend (significant at 95%) and variability of (a) IVT300 (b) IVT (c) specific humidity (d) zonal wind (e) meridional wind of different layers in the central north Atlantic (30oN-60oN, 80oW-0).

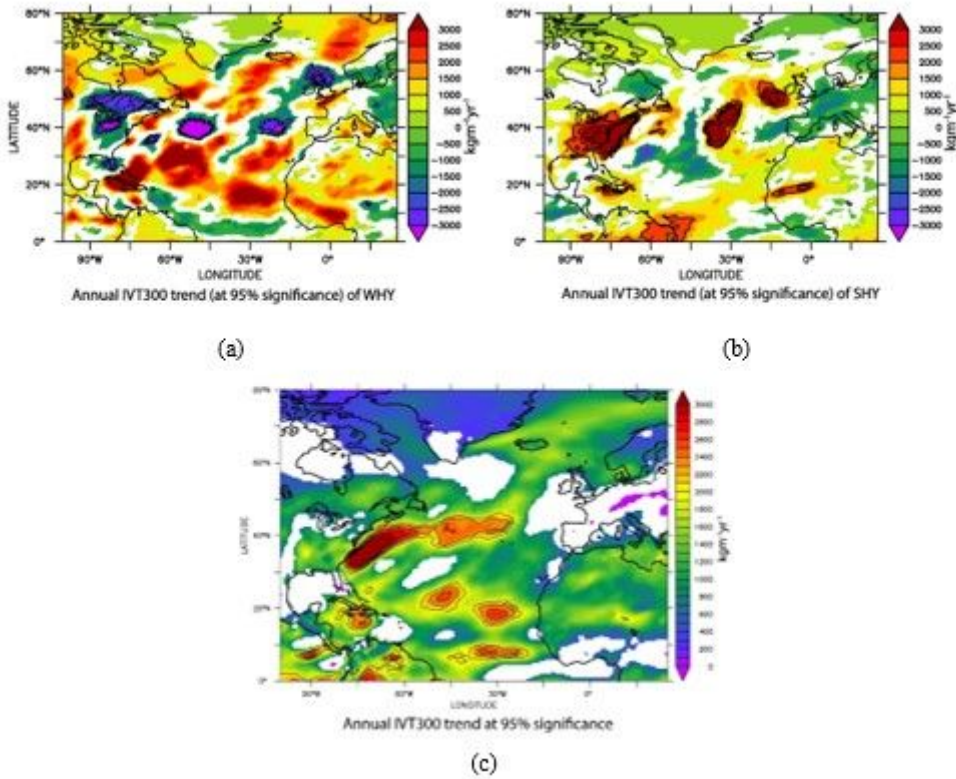


Figure 8

Spatial trend analysis during (a) WHY (b) SHY and (c) Annual using daily IVT300 (at 95% significance).

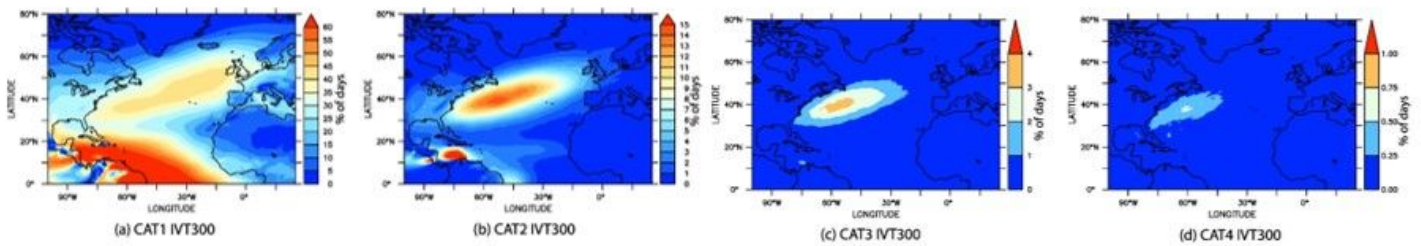


Figure 9

Spatial frequency analysis of different categories of daily IVT300.

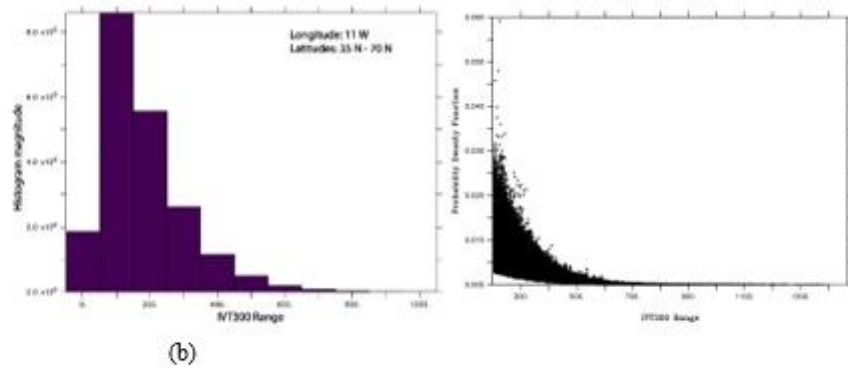


Figure 10: (a) Histogram and (b) probability density function of daily IVT300 along 11°W.

Figure 10

(a) Histogram and (b) probability density function of daily IVT300 along 11°W.

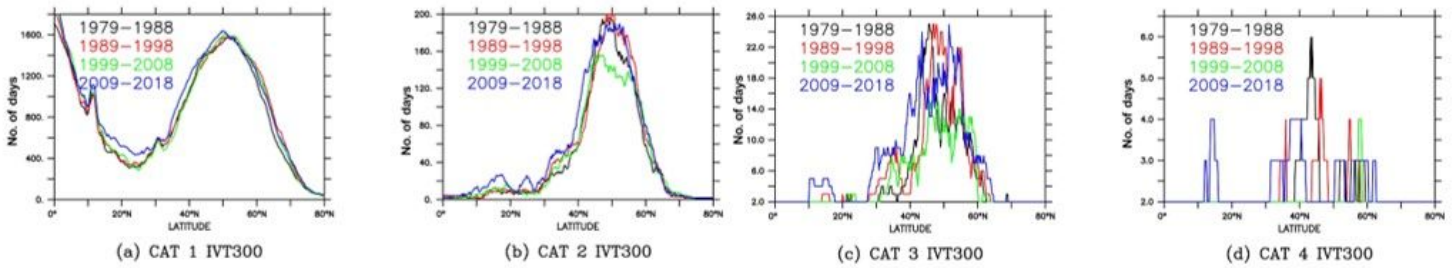


Figure 11

Frequency of daily IVT300 along 11°W.

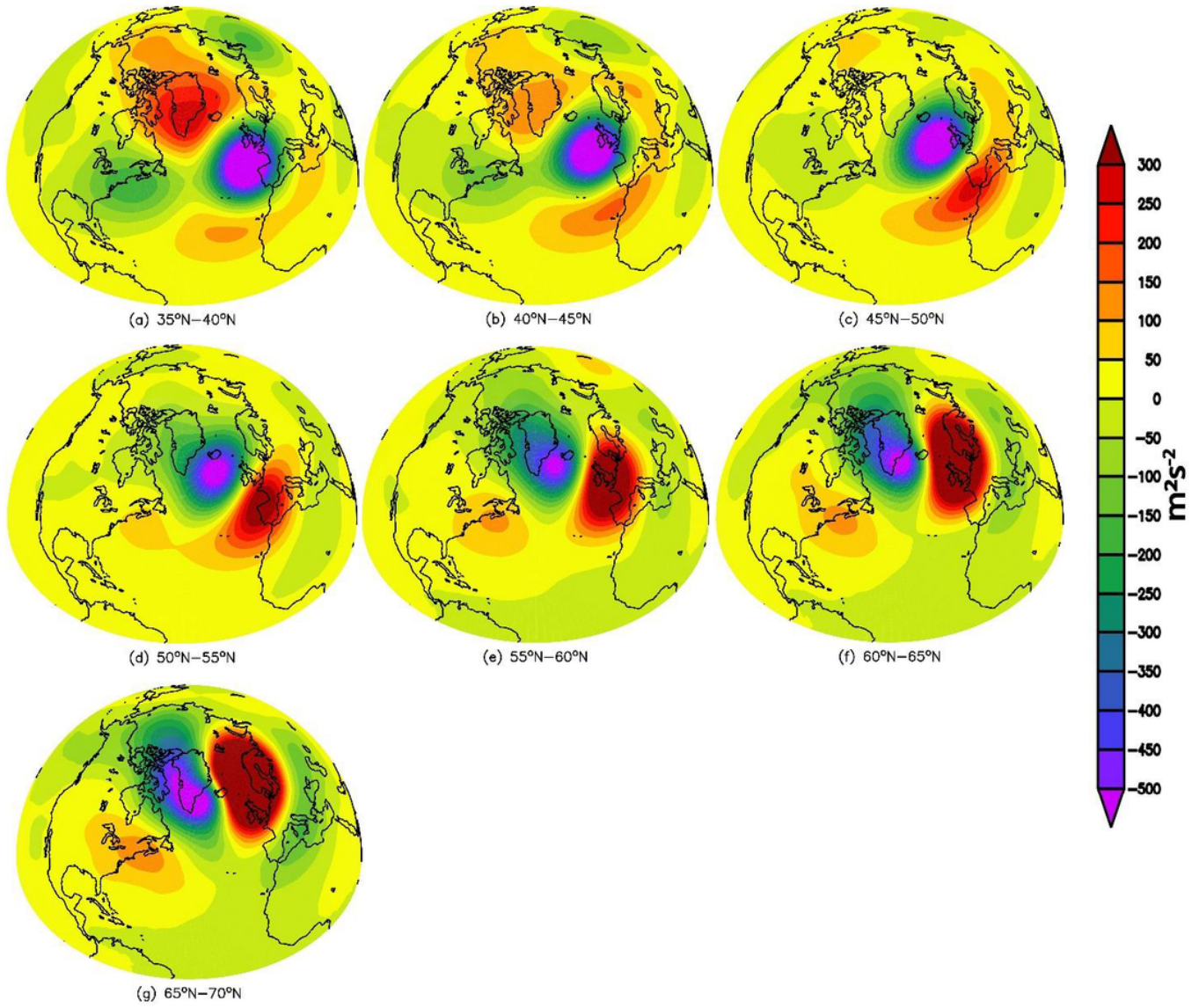


Figure 12

Composite of geopotential anomaly along 110W using different bins

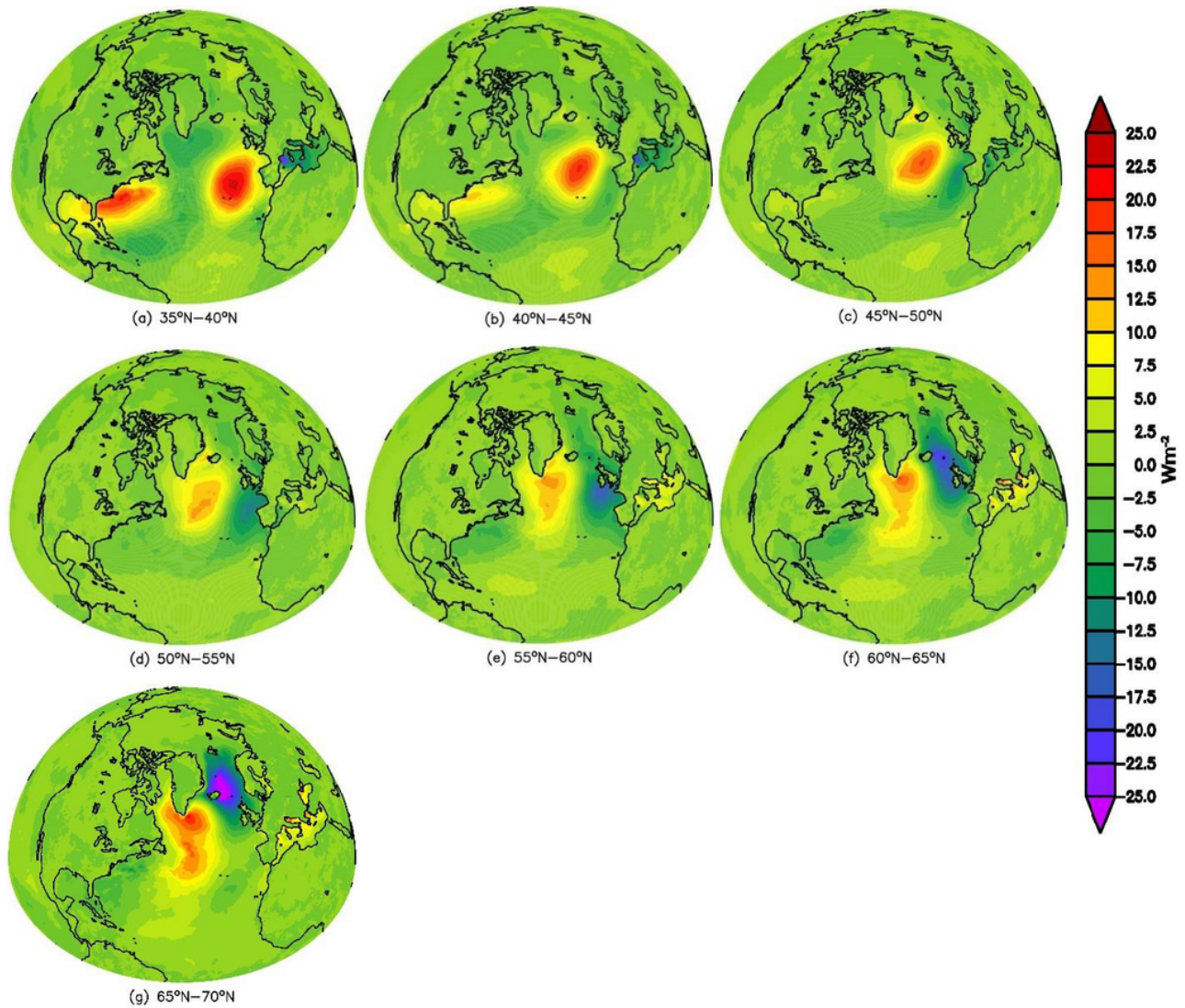


Figure 13

Composite of surface latent heat flux anomaly along 11°W using different bins

Supplementary Files

This is a list of supplementary files associated with this preprint. Click to download.

- [FigureS1.jpg](#)
- [FigureS2.jpg](#)
- [FigureS3.jpg](#)